



Insights into the Properties of Type Ibn/Icn Supernovae and Their Progenitor Channels through X-Ray Emission

Yusuke Inoue and Keiichi Maeda

Department of Astronomy, Kyoto University, Kitashirakawa-Oiwake-cho, Sakyo-ku, Kyoto, 606-8502, Japan; yusuke@kustro.kyoto-u.ac.jp

Received 2024 October 1; revised 2024 December 7; accepted 2024 December 10; published 2025 February 5

Abstract

Type Ibn/Icn supernovae (SNe Ibn/Icn), which are characterized by narrow helium or carbon lines that originated in hydrogen-poor dense circumstellar medium (CSM), provide new insights into the final evolution of massive stars. While SNe Ibn/Icn are expected to emit strong X-rays through the strong supernova (SN)–CSM interaction, the X-ray emission modeling effort has been limited so far. In the present study, we provide broad-band X-ray light curve (LC) predictions for SNe Ibn/Icn. We find that the soft X-ray LC provides information about the CSM compositions, while the hard X-ray LC is a robust measure of the CSM density, the explosion energy, and the ejecta mass. In addition, considering the evolution of the ionization state in the unshocked CSM, a bright soft X-ray is expected in the first few days since the explosion, which encourages rapid X-ray follow-up observations as a tool to study the nature of SNe Ibn/Icn. Applying our model to the soft X-ray LCs of SNe Ibn 2006jc and 2022ablq, we derive that the CSM potentially contains a larger fraction of carbon and oxygen for SN 2006jc than 2022ablq, highlighting the power of the soft X-ray modeling to address the nature of the CSM. We also discuss detectability and observational strategy, with which the currently operating telescopes such as NuSTAR and Swift can offer an irreplaceable opportunity to explore the nature of these enigmatic rapid transients and their still-unclarified progenitor channel(s).

Unified Astronomy Thesaurus concepts: [Circumstellar matter \(241\)](#); [Stellar evolution \(1599\)](#); [X-ray transient sources \(1852\)](#)

1. Introduction

Massive stars with a zero-age main-sequence mass (M_{ZAMS}) exceeding $\sim 8M_{\odot}$ trigger terminal explosions are called core-collapse supernovae (CCSNe). Most of them show broad lines corresponding to the ejecta velocity of $\sim 10^4 \text{ km s}^{-1}$ in their spectra, while some supernovae (SNe) show narrow lines. For example, Type IIn SNe (SNe IIn) show narrow hydrogen (H) lines (A. V. Filippenko 1997). The narrow lines are believed to form in the dense circumstellar medium (CSM) with a velocity of $\sim 10^2 \text{ km s}^{-1}$ (e.g., N. Smith 2014, 2017). The collision of supernova (SN) ejecta with such dense CSM efficiently dissipates the kinetic energy, leading to strong emissions across the multiwavelengths (e.g., optical, radio, and X-ray; E. O. Ofek et al. 2007, 2014; N. Smith et al. 2007; P. Chandra et al. 2012; M. Stritzinger et al. 2012; C. Fransson et al. 2014). This picture of the SN–CSM interaction model for SNe IIn has been well established (e.g., R. A. Chevalier 1982; R. A. Chevalier & C. Fransson 2003, 2017).

Their CSM distribution reflects the mass-loss history before the SN explosion. For SNe IIn, the optical light-curve (LC) modeling based on the SN–CSM interaction model (e.g., T. J. Moriya et al. 2013, 2014) has indicated extreme mass-loss rates of $10^{-4}M_{\odot} \sim 1M_{\odot} \text{ yr}^{-1}$ within $\sim 100 \text{ yr}$ toward the explosion. Such LC analyses provide valuable opportunities for revealing stellar evolution and explosion properties.

There are several variants in the family of interacting SNe. SNe Ibn show narrow helium (He) lines and likely have He-

rich CSM; SNe Icn show narrow carbon (C) lines and likely have C-rich CSM. The widths of these helium and carbon lines correspond to the CSM velocity of $\sim 10^3 \text{ km s}^{-1}$ (A. Pastorello et al. 2007; I. Shivvers et al. 2016; 2017; G. Hosseinzadeh et al. 2017; D. A. Perley et al. 2022; C. Pellegrino et al. 2022a; A. Gal-Yam et al. 2022; T. Nagao et al. 2023; K. W. Davis et al. 2023; M. Pursiainen et al. 2023). The progenitors of SNe Ibn/Icn might have undergone a more extreme mass-loss episode than the progenitors of SNe IIn, with the mass loss reaching down to the inner He or even C layer (e.g., A. Pastorello et al. 2007; A. Gal-Yam et al. 2022).

The optical LCs of SNe Ibn/Icn show a rapid decline. It has been interpreted that SNe Ibn/Icn are mainly powered by the SN–CSM interaction with a steep CSM density profile (T. J. Moriya & K. Maeda 2016; K. Maeda & T. J. Moriya 2022; T. Nagao et al. 2023). The steep CSM profile translates into the mass-loss rate of the progenitor increasing toward the explosion. This may provide a clue to the still-unclarified mechanism(s) of such pre-SN activity (e.g., R. J. Foley et al. 2007; N.-C. Sun et al. 2020; K. Maeda & T. J. Moriya 2022; S. J. Brennan et al. 2024).

However, the optical LC modeling involves relatively large uncertainties (e.g., A. Gangopadhyay et al. 2020; C. Pellegrino et al. 2022b) since the optical emission is an outcome of reprocessing the originally emitted X-ray photons to optical photons through various processes such as Compton scattering. The X-ray emission can provide a more direct view than the optical emission, on the properties of the CSM and SN ejecta; the temperatures behind forward shock (FS) and reverse shock (RS) correspond to the X-ray energy range.

The X-ray observation of SNe Ibn/Icn has been limited due to their rarity and rapidly evolving nature. The only two cases

with the reported X-ray detection are SNe Ibn 2006jc (S. Immler et al. 2008) and 2022ablq (C. Pellegrino et al. 2024),¹ and there are a few cases where upper limits are placed, e.g., SN Icn 2019hgp (A. Gal-Yam et al. 2022). However, once obtained, the X-ray data provide powerful diagnostics; for SN 2006jc, N. N. Chugai (2009) extracted the properties of the CSM through the X-ray LC modeling. The present work aims at promoting/accelerating X-ray observations of SNe Ibn/Icn, by providing the X-ray model that can be directly applied to such data.

This paper is structured as follows. The methods of our X-ray LC modeling are described in Section 2. The results are presented in Section 3. In Section 4, we apply our model to SNe 2006jc, 2019hgp, and 2022ablq. In Section 5, additional discussion is given on the evolution of the ionization state in the unshocked CSM. The importance of hard X-ray observations and a caveat in our X-ray LC model is described in Section 6. Our findings are summarized in Section 7.

2. Methods

We assume that SNe Ibn/Icn are powered solely by the SN-CSM interaction, and omit possible contribution by radioactive decay (e.g., R. J. Foley et al. 2007; K. Maeda & T. J. Moriya 2022). Behind the FS and the RS, the gas temperatures immediately after the shock heating are $\sim 10^9$ K and 10^7 K, respectively (R. A. Chevalier & C. Fransson 2003, 2017; K. Maeda & T. J. Moriya 2022). The X-ray emission process behind the FS and the RS is dominated by free–free emission and line emission, respectively. In this section, we describe our methods to calculate the X-ray LCs for SNe Ibn/Icn.

2.1. Hydrodynamics for the SN-CSM Interaction

Hydrodynamics for the SN-CSM interaction is simulated in 1D spherical symmetric geometry, adopting the open-source code The Supernova Explosion Code (SNEC; V. Morozova et al. 2015). The input parameters are the following: ejecta mass (M_{ej}), ejecta (kinetic) energy ($E_{\text{kin,ej}}$), and the CSM density (ρ_{CSM}). The initial ejecta structure as a function of radius (r) is assumed to follow the homologous expansion (R. A. Chevalier & C. Fransson 2003, 2017), as represented by a broken power-law function; each segment is described as $\rho_{\text{ej}} \propto r^{-n}$, where $n = 0$ for the inner part and 7 for the outer part (assuming a compact-star progenitor like a Wolf–Rayet star; N. Tominaga et al. 2008). The radial distribution of the CSM density is assumed to follow a single power-law function as $\rho_{\text{CSM}} = 10^{-14} D' (r/5 \times 10^{14} \text{ cm})^{-s} \text{ g cm}^{-3}$ (see K. Maeda & T. J. Moriya 2022). Here, the D' is a constant parameter that controls the density scale. This is the same setup used in the previous studies on optical LC modeling (K. Maeda & T. J. Moriya 2022; T. Nagao et al. 2023).

A typical range of the parameters we investigate is the following. For SNe Ibn, $M_{\text{ej}} = 2\text{--}6M_{\odot}$, $E_{\text{kin,ej}} \sim 10^{51} \text{ erg}$ ($= 1 \text{ Bethe(B)}$), $D' \sim 0.5\text{--}5.0$, and $s \sim 3$ (K. Maeda & T. J. Moriya 2022). For SNe Icn, the parameters are similar to

those of SNe Ibn, while the ejecta energy may be higher (a few B; T. Nagao et al. 2023).

With the setup described above, we first calculate the SN-CSM interaction with the adiabatic hydrodynamic mode of SNEC. The radiative cooling by free–free and line emissions, as well as the energy exchange between electrons and ions, are incorporated as a post-process. As the initial condition of the thermal energy evolution of ions, we adopt the gas properties (e.g., gas density and gas temperature) given by the SNEC simulation. Subsequently, we calculate the thermal energy evolution of ions and electrons as described below. For each mass element, the time evolutions of the thermal energy of electrons and that of ions ($\frac{dE_{\text{th,e}}}{dt}$, $\frac{dE_{\text{th,ion}}}{dt}$) are computed as follows:

$$\frac{dE_{\text{th,e}}}{dt} = \frac{dE_{\text{ad,th,e}}}{dt} - L_X(t) + P_{\text{e-ion}}, \quad (1)$$

$$\frac{dE_{\text{th,ion}}}{dt} = \frac{dE_{\text{ad,th,ion}}}{dt} - P_{\text{e-ion}}, \quad (2)$$

where $\frac{dE_{\text{ad,th},i}}{dt}$ ($i = \text{e, ion}$) expresses the time evolution of the thermal energy of electrons or ions in the mass element, only taking into account the contribution from the adiabatic expansion cooling and the shock heating. In computing the X-ray luminosity (i.e., radiative cooling), L_X , we take into account free–free emission and line emissions (see Section 2.2 for details). Practically, we place a limit on L_X so that the internal energy does not become negative. The term $P_{\text{e-ion}}$ expresses the energy transfer from ions to electrons. In Equation (2), we treat the gas including various ions as a single-temperature component.

Using Equations (1) and (2) and the Ideal single-particle Boltzmann gas EOS with the output from the adiabatic hydrodynamics simulations by SNEC, the electron and ion temperatures (T_e , T_{ion}) in the downstream of a shock wave are calculated. The ratio of specific heats is chosen to be 5/3.

The adiabatic term is expressed as follows:

$$\frac{dE_{\text{ad,th},i}}{dt} = \begin{cases} \frac{dE_{\text{ad,th}}}{dt} \frac{n_i}{n_{\text{ion}} + n_e} & (\text{shock front}) \\ \frac{dE_{\text{ad,th}}}{dt} \frac{T_i}{T} \frac{n_i}{n_{\text{ion}} + n_e} & (\text{downstream of the shock}) \end{cases}. \quad (3)$$

The gas temperature taken from the adiabatic hydrodynamics simulations by SNEC is denoted by T , while the electron and ion temperatures computed through the post-process are expressed by T_e and T_{ion} . The n_e and n_{ion} are the number density of free electrons and that of ions, respectively (see Section 2.3 for the treatment of the ionization state). The upper term of Equation (3) includes the contributions from the shock heating and the ion–electron energy exchange, assuming that the energy exchange between electrons and ions is immediately completed at the shock front. This is a rational assumption since the relaxation timescale between electrons and ions is much shorter than the dynamical timescale under the situation considered here (see R. A. Chevalier & C. Fransson 2003, 2006; K. Maeda & T. J. Moriya 2022). The factor $\frac{n_i}{n_{\text{ion}} + n_e}$ takes into account the contribution of free electrons to the time evolution of thermal energy ($\frac{dE_{\text{ad,th}}}{dt}$) in the adiabatic hydrodynamics simulation by SNEC. The lower term of Equation (3) describes the adiabatic expansion cooling of electrons. The factor $\frac{T_i}{T}$ is introduced to correct for the effect of

¹ In the present study, we adopt the data points of SN 2022ablq from the arXiv version of C. Pellegrino et al. (2024), which are slightly different from the data points presented in the published version. We have confirmed that the difference is sufficiently small for our purpose, and does not affect our conclusions; if we adopt the data points from their published version, our model results in $D' = 5.2$ and $(\text{He, C, O}) = (0.97, 0.015, 0.015)$, with the other parameters unchanged.

the adiabatic cooling after taking into account the radiative cooling of electrons.

The electron-ion energy-exchange rate, $P_{e\text{-ion}}$, is expressed as follows (see Equation (5) in H. Itoh (1977) and Equation (26) in R. A. Chevalier & C. Fransson 2006):

$$P_{e\text{-ion}} = \frac{3\bar{Z}}{2} \frac{\ln\Lambda}{4 \cdot 4.2 \times 10^{-22}} k_B (T_{\text{ion}} - T_e) n_e \rho T_e^{-1.5}, \quad (4)$$

where \bar{Z} , $\ln\Lambda \approx 30$, k_B , and ρ are the average charge of the ions, the Coulomb logarithm, the Boltzmann's constant, and the mass density of the gas given by the SNEC simulation. In our reference model (Section 3), $\bar{Z} \approx 3$ corresponding to (He, C, O) = (0.5, 0.25, 0.25) in the mass fraction. At the shock front, we set this as $P_{e\text{-ion}} = 0$ because Equation (3) already includes the effect of $P_{e\text{-ion}}$ there.

After the calculation of the thermal energy evolution, the X-ray luminosity at a given energy band is calculated considering absorption processes such as Compton scattering and photoelectric absorption (see Section 2.3). We note that our model for the internal energy evolution does not include the feedback effect of the radiation loss on hydrodynamics, but we confirm that this treatment represents a good first approximation (see Appendix A).

2.2. X-Ray Emission Process

The X-ray emission from SNe Ibn/Icn is dominated by that arising from the FS for the following reasons. Because of the dense CSM, the RS is ineffective in producing X-ray emission for at least a few hundred days; the X-ray emission from the RS is mainly in the soft X-ray band ($\sim 0.1\text{--}10$ keV), and initially, the soft X-rays are almost entirely absorbed by photoelectric absorption in the cooled shocked ejecta behind the RS (see Sections 2.3 and 3.1). Also, the cooling is so effective behind the RS, and the RS region is rapidly cooled down; thus, little X-ray emission is expected from the RS. The cooling in the FS region is much slower than the RS region due to the much higher temperature; when the time evolution of the thermal energy (Equation (1)) is calculated, the line emission is taken into account using the fitting formula for the cooling function presented by R. A. Chevalier & C. Fransson (2003, 2017), but it is inefficient at $\sim 10^9$ K. Therefore, free-free emission from the FS region is dominant in the entire X-ray bands covering the soft (< 10 keV) and hard (> 10 keV) X-rays, and we compute the X-ray spectral energy distribution (SED) under this assumption.

The emissivity of free-free emission is expressed as follows (G. B. Rybicki & A. P. Lightman 1979):

$$\epsilon_\nu^{\text{ff}} = 6.84 \times 10^{-38} g_{\text{ff}} T_e^{-0.5} n_e \sum_j Z_j^2 n_j \exp\left(-\frac{E_{\text{ph}}}{k_B T_e}\right), \quad (5)$$

where g_{ff} , Z_j , n_j , and E_{ph} are the Gaunt factor, the atomic number of element j , the number density of element j , and the photon energy. n_e and n_j are calculated using the mass density of the gas (see Section 2.3 for the treatment of the ionization state). The Gaunt factor g_{ff} is fixed to be 1 for simplicity.

2.3. X-Ray Absorption Processes

From the optical spectra of SNe Ibn/Icn, it is believed that they have H-poor CSM (e.g., A. Pastorello et al. 2007; A. Gal-Yam et al. 2022). We assume that the CSM is

composed of elements heavier than H, such as He, C, oxygen (O), neon (Ne), and magnesium (Mg), and set their mass fractions guided by previous studies and stellar evolution simulations (K. Nomoto & M. Hashimoto 1988; N. Tominaga et al. 2008). For example, N. N. Chugai (2009) and S. Mattila et al. (2008) have chosen (He, C, O) \sim (0.73, 0.14, 0.13) as the mass fractions. In the present study, we investigate X-ray emission from SNe Ibn and Icn. Therefore, we choose a wide range of CSM compositions (see Sections 3.1 and 4.2).

The ionization state in the shocked region is modeled as follows, assuming that collisional ionization is the main ionization process (see D. P. Cox & W. H. Tucker 1969, for details). We treat all atoms as effectively neutral at $T_e < 10^4$ K; at $T_e = 10^4\text{--}10^6$ K, He is fully ionized, and the others are He-like ions; at $T_e = 10^6\text{--}10^7$ K, He, C, and O are fully ionized, and the others are He-like ions; at $T_e > 10^7$ K, all atoms are fully ionized. The results of LCs are not sensitive to this assumption on the ionization state in the shocked region. This is because the temperature in the region behind the FS is $\sim 10^9$ K; thus, all atoms (even iron (Fe)) can be assumed to be fully ionized. On the other hand, we assume that atoms in the unshocked CSM are (effectively) neutral in Sections 3 and 4 (see Section 5 for the effect of photoionization in the unshocked CSM).

We consider Compton scattering and photoelectric absorption as absorption processes for X-rays. We use the angle-averaged Klein–Nishina's formula (G. B. Rybicki & A. P. Lightman 1979) for Compton scattering. Photoelectric absorption is calculated using the open database `xlaylib` (A. Brunetti et al. 2004; T. Schoonjans et al. 2011). `xlaylib` provides the opacities of photoelectric absorption for neutral and ground-state atoms. We treat ions that are not fully ionized as neutral atoms in the calculation of absorption. The resulting LCs are not sensitive to this assumption, since the photoelectric absorption is mainly contributed by electrons in the K shell of ions.

The total opacity of photoelectric absorptions by all ions ($\kappa_{\text{pe,total}}(E_{\text{ph}})$), for photons with E_{ph} , is described as follows:

$$\kappa_{\text{pe,total}}(E_{\text{ph}}) = \sum_j Y_j \kappa_{\text{pe},j}(E_{\text{ph}}), \quad (6)$$

where Y_j is the mass fraction of element j . For fully ionized elements, Y_j is set to be 0. In the above equation, $\kappa_{\text{pe},j}(E_{\text{ph}})$ is the opacity of photoelectric absorption by neutral atom j for photons with E_{ph} , and this is given by `xraylib`.

The total opacity at E_{ph} in each mass element is then expressed as follows:

$$\kappa(E_{\text{ph}}) = \kappa_{\text{pe,total}}(E_{\text{ph}}) + \kappa_{\text{Comp}}(E_{\text{ph}}), \quad (7)$$

where $\kappa_{\text{Comp}}(E_{\text{ph}})$ is the opacity of Compton scattering. Compton scattering dominates the opacity in the FS region, while photoelectric absorption is the most important in the RS region. Indeed, the unshocked CSM is the main contributor to the photoelectric absorption. Therefore, we consider Compton scattering only in the FS region.

For X-rays emitted from each mass element, the observed luminosity ($L_{X,\text{obs}}(E_{\text{ph}})$) is expressed as follows:

$$L_{X,\text{obs}}(E_{\text{ph}}) = 0.5 L_X(E_{\text{ph}}) \exp(-\tau(E_{\text{ph}})), \quad (8)$$

$$\tau(E_{\text{ph}}) = \int_{r_{\text{emi}}}^{\infty} \kappa(E_{\text{ph}}) \rho dr. \quad (9)$$

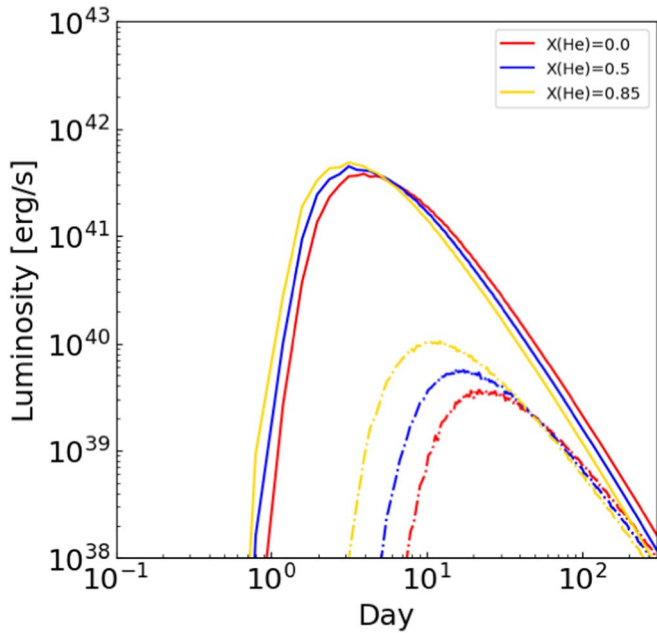


Figure 1. The dependence of the synthetic hard (10–40 keV; solid) and soft (0.2–10 keV; dashed-dotted) X-ray LCs on the CSM composition. Shown here are the models with $X(\text{He}) = 0$ (red), 0.5 (blue), and 0.85 (yellow).

Here, the r_{emi} is where the radiation $L_X(E_{\text{ph}})$ is emitted. The factor of 0.5 in Equation (8) comes from our assumption that half of the isotropically emitted X-rays go outward following Equation (8) while the other half goes inward, a frequently adopted assumption in such analyses (e.g., R. A. Chevalier & C. Fransson 2003; K. Maeda & T. J. Moriya 2022). The X-rays that go inward are converted into low-energy photons (e.g., optical or UV) in the SN ejecta.

3. General Properties of X-Ray LCs with Neutral Unshocked CSM

In this section, we examine the parameter dependence of our X-ray LC model under the assumption that the unshocked CSM is effectively neutral (i.e., not fully ionized). We adopt $M_{\text{ej}} = 2 M_{\odot}$, $E_{\text{kin ej}} = 1\text{B}$, $V_{\text{CSM}} = 1000 \text{ km s}^{-1}$, $s = 3$, $D' = 1.6$, and $(\text{He}, \text{C}, \text{O}) = (0.5, 0.25, 0.25)$ for the CSM composition, unless specifically mentioned. The CSM velocity (V_{CSM}) is assumed to be 1000 km s^{-1} , as is typically measured from the narrow lines of SNe Ibn/Icn.

3.1. Soft X-Ray Properties

The property of the soft X-ray strongly reflects the CSM composition through photoelectric absorption ($\kappa_{\text{pe}} \propto E_{\text{ph}}^{-3.5}$ for the K-shell approximation; M. S. Longair 2011). Here, we adopt He, C, and O as representative elements in the CSM. A model with $(\text{He}, \text{C}, \text{O}) = (0.5, 0.25, 0.25)$ is taken as a reference model, while additional models are examined with $(\text{He}, \text{C}, \text{O}) = (0.85, 0.03, 0.12)$ (helium-envelope composition) and $(\text{He}, \text{C}, \text{O}) = (0.0, 0.5, 0.5)$ (carbon layer composition).

Figure 1 shows the synthetic X-ray LCs. For the lower fraction of the heavy elements, the X-ray LC peaks earlier with a higher peak luminosity because of the metallicity dependence of $\kappa_{\text{pe},j}$ ($\kappa_{\text{pe},j} \propto Z_j^5$ for the K-shell approximation; M. S. Longair 2011).

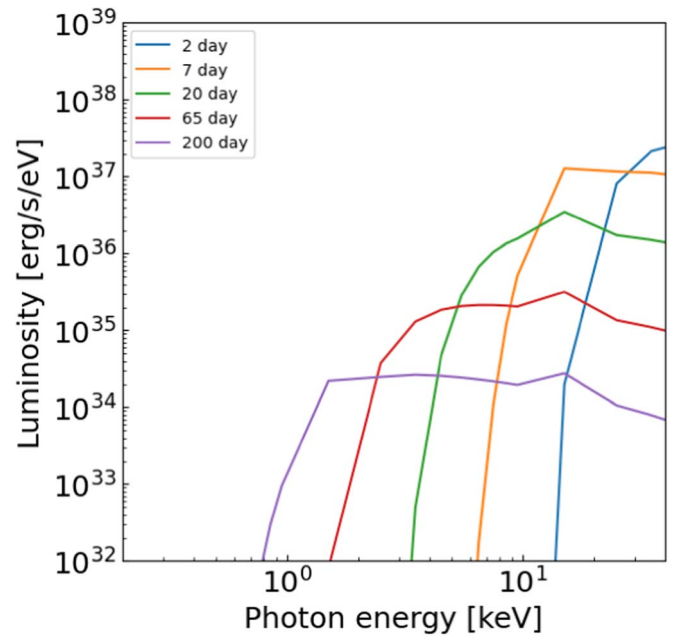


Figure 2. The SED evolution for the model with $(\text{He}, \text{C}, \text{O}) = (0.5, 0.25, 0.25)$. The blue, orange, green, red, and violet solid lines show the SED at 2, 7, 20, 65, and 200 days since the explosion, respectively.

Figure 2 shows the evolution of the SED of the reference model with $X(\text{He}) = 0.5$. At a higher energy, the system becomes optically thin more rapidly. The soft X-ray reaches a fainter peak luminosity than the hard X-ray. These are general trends for SNe Ibn/Icn, arising from a combination of the stronger photoelectric absorption at a lower X-ray energy range (see Figure 3) and the decreasing SN-CSM interaction power. We note that the contribution of X-ray emission from RS can be ignored because the optical depth in the cooled shocked ejecta behind the RS is much larger than those of the FS and CSM.

3.2. Hard X-Ray Properties

The CSM composition dependence of the hard X-ray LC is weaker than that of the soft X-ray LC (see Figure 1). Figure 4 shows the synthetic X-ray LCs with various ejecta properties ($E_{\text{kin ej}}$ and M_{ej}). With a higher ejecta velocity, the X-ray LC peaks earlier at a higher peak luminosity. This is because the system, including both the shocked and unshocked CSMs, rapidly becomes optically thin for a faster shock wave.

Figure 5 shows the synthetic X-ray LCs with various CSM densities (D'). For a higher CSM density, the hard X-ray emerges later and peaks at a higher luminosity; this is a result of the increasing optical depth ($\tau \propto \rho$) and emissivity ($\epsilon_{\nu}^{\text{ff}} \propto \rho^2$) for a higher density. We note that the rising phase of the hard X-ray LCs is not smooth, but this is a numerical artifact; our shortest time step in the LC simulations is $\sim 10^{-2}$ – 10^{-1} days.

The hard X-ray LC generally peaks earlier than the soft X-ray LC because the optical depth for the hard X-rays is smaller than that for the soft X-rays. Therefore, there is a period when the rising phase of the soft X-ray LC and the decay phase of the hard X-ray overlap. The decay phase of the hard X-ray LC provides a robust measure of the CSM density irrespective of the evolution in the soft X-ray LC. With the CSM density thus anchored by the hard X-ray properties, the analysis of the

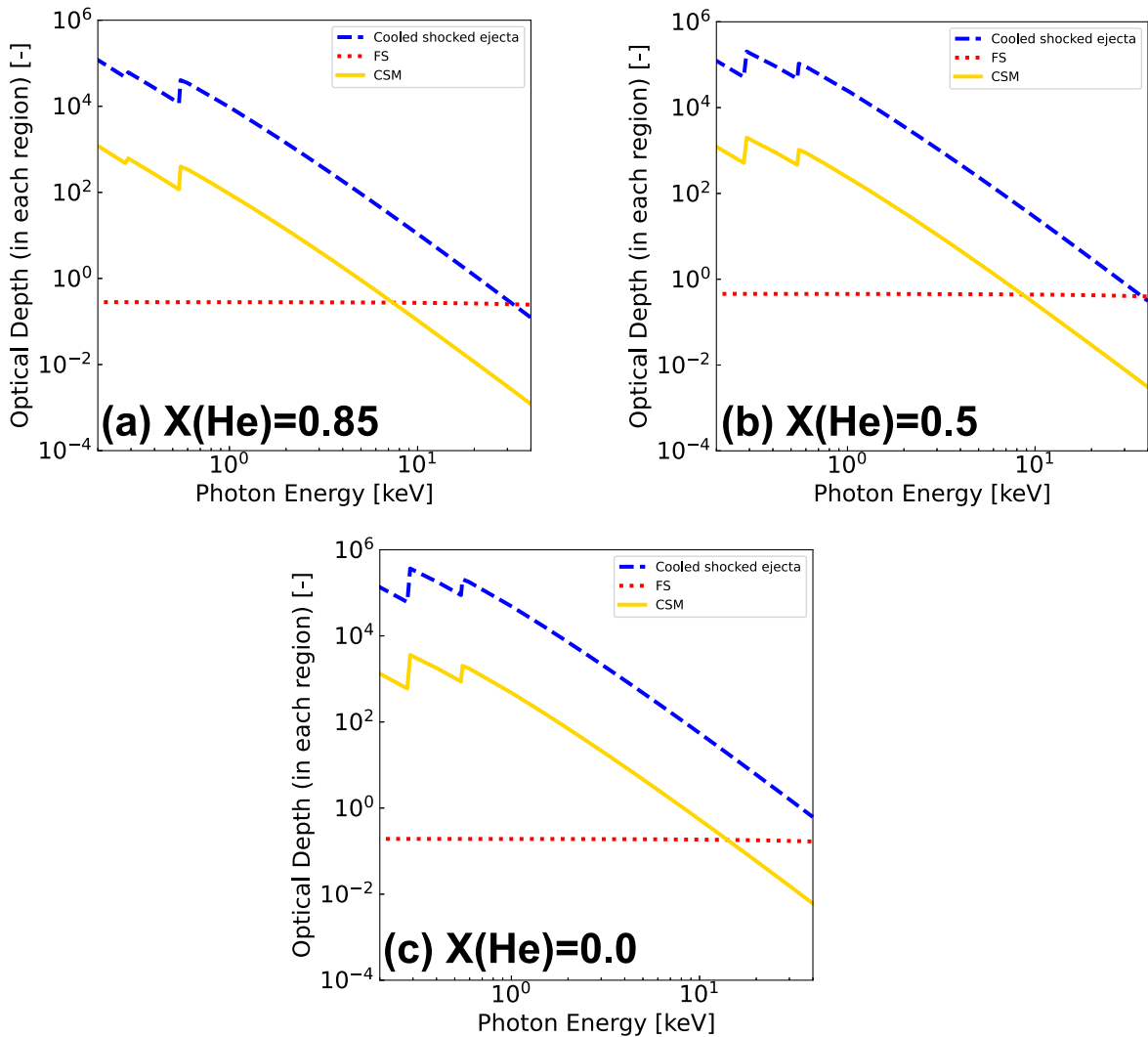


Figure 3. The dependence of the optical depth on the CSM composition. (a) $X(\text{He}) = 0.85$, (b) $X(\text{He}) = 0.5$, and (c) $X(\text{He}) = 0$. Shown here are the optical depth of Compton scattering within the region shocked by the FS (dotted), that of photoelectric absorption within the unshocked CSM (solid), and that of photoelectric absorption within the cooled shocked ejecta (dashed).

rising phase of the soft X-ray LC can then provide the information on the CSM composition separately, i.e., the degeneracy between the CSM density and composition could be solved by these properties (see also Section 6.1).

4. Application to Individual Objects

4.1. SN 2006jc

Figure 6 shows the synthetic X-ray LCs (with effectively neutral CSM; see Section 5) as compared to the data of SN 2006jc. The physical parameters adopted here are $M_{\text{ej}} = 6M_{\odot}$, $E_{\text{kin ej}} = 0.8B$, $V_{\text{CSM}} = 3000 \text{ km s}^{-1}$, $s = 3$, and $D' = 4.0$. The CSM velocity corresponds to the typical width of the helium emission lines seen in SN 2006jc (R. J. Foley et al. 2007; A. Pastorello et al. 2007, 2008). As a reference model, we adopt $(\text{He}, \text{C}, \text{O}) = (0.73, 0.14, 0.13)$ in the mass fractions; this represents the composition in the helium layer and was adopted in the previous studies (N. N. Chugai 2009; S. Mattila et al. 2008). Additionally, we examine the case with $(\text{He}, \text{C}, \text{O}) = (0.4, 0.3, 0.3)$, corresponding to the deeper part of the progenitor toward the carbon layer (e.g., K. Nomoto & M. Hashimoto 1988; N. Tominaga et al. 2008). We set the

number fraction of carbon larger than that of oxygen in our models; the infrared (IR) spectral evolution of SN 2006jc suggested that carbon grains were formed in the shocked CSM (e.g., N. Tominaga et al. 2008; I. Sakon et al. 2009) which requires a larger number density of carbon than oxygen (T. Nozawa et al. 2008).

The model with $(\text{He}, \text{C}, \text{O}) = (0.4, 0.3, 0.3)$ explains the rising phase of SN 2006jc better than the He-rich composition, indicating a nearly complete stripping of the He envelope (see Appendix B about robustness in deriving the CSM composition). However, we refrain from deriving a strong conclusion from this result since it is sensitive to the assumed CSM density; our model is based on the optical LC modeling by K. Maeda & T. J. Moriya (2022), but the optical LC modeling may involve several uncertainties and possible systematic errors. Rather, we emphasize that the robustly determined CSM density profile is needed to derive the CSM abundance. This is where the hard X-ray observation can play a key role (see Sections 3.2 and 6.1).

In this section, photoionization in the unshocked CSM is not considered, and it is assumed that the CSM is not fully ionized. We will show in Section 5 that this assumption is appropriate

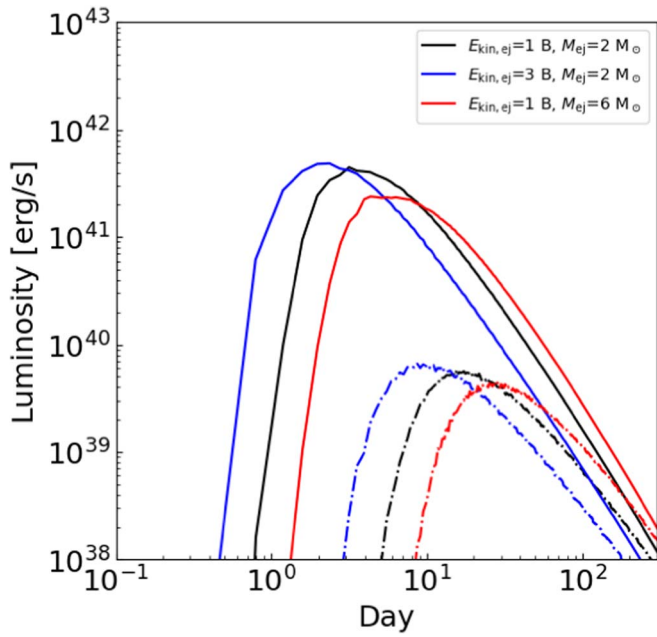


Figure 4. The dependence of the synthetic hard (10–40 keV; solid) and soft (0.2–10 keV; dashed–dotted) X-ray LCs on the ejecta properties. Shown here are the models with $E_{\text{kin,ej}} = 1\text{B}$ and $M_{\text{ej}} = 2 M_{\odot}$ (black), 3B and $2 M_{\odot}$ (blue), and 1B and $6 M_{\odot}$ (red).

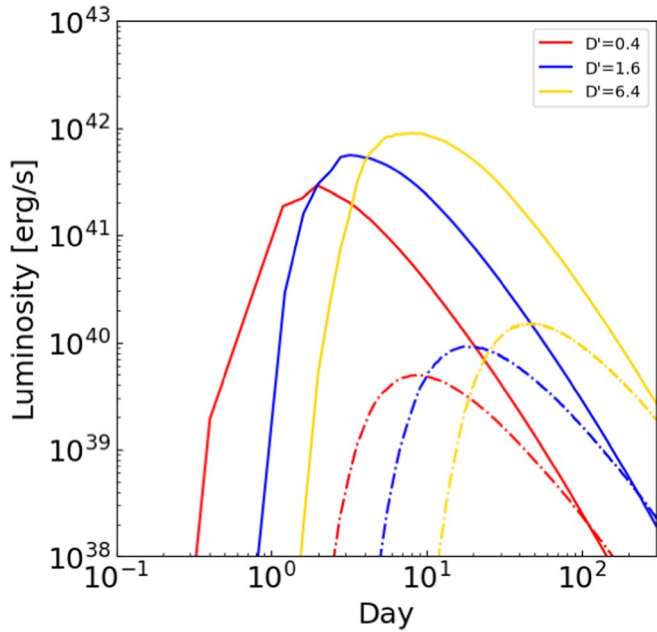


Figure 5. The dependence of the synthetic hard (10–40 keV; solid) and soft (0.2–10 keV; dashed–dotted) X-ray LCs on the CSM density. Shown here are the models with $D' = 0.4$ (red), 1.6 (blue), and 6.4 (yellow).

at $\gtrsim 1$ day since the explosion for SN 2006jc. Therefore, the parameters derived in this section would not be affected by the treatment of the ionization status of the unshocked CSM.

4.2. SN 2019hgp

SN 2019hgp is one of the first SNe Icn reported in the literature (A. Gal-Yam et al. 2021, 2022). SN 2019hgp was observed with Swift but not detected in 0.3–10 keV during ~ 1.5 –57 days since the explosion. We adopt the upper limits

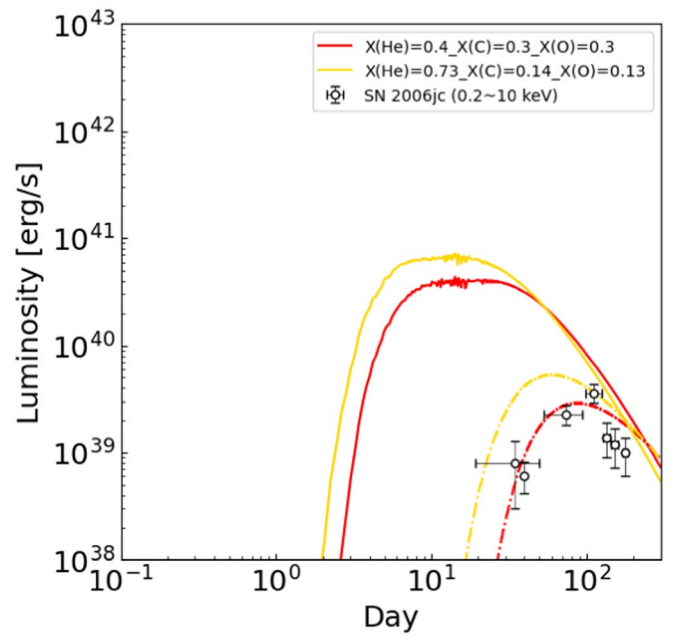


Figure 6. The synthetic hard (10–40 keV; solid) and soft (0.2–10 keV; dashed–dotted) X-ray LCs for SN 2006jc with the (effectively) neutral unshocked CSM, as compared to the X-ray data of SN 2006jc. Shown here are the models with (He, C, O) = (0.4, 0.3, 0.3) (red) and (0.73, 0.14, 0.13) (yellow). The data points are from S. Immler et al. (2008).

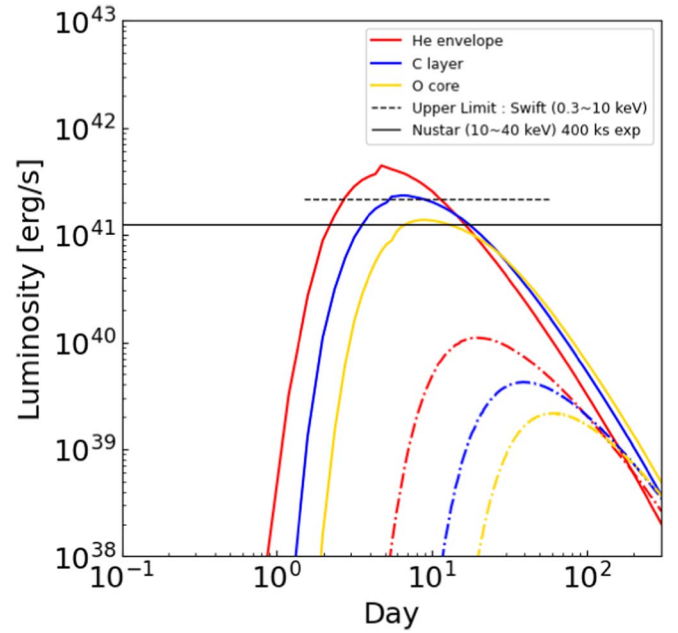


Figure 7. The hard (10–40 keV; solid) and soft (0.2–10 keV; dashed–dotted) synthetic X-ray LCs for SN 2019hgp, with different CSM compositions. Shown here are the models with He-envelope compositions (red), the C-layer compositions (blue), and the O-core compositions (yellow). The black-dashed horizontal line represents the soft X-ray upper limit (3σ) taken from A. Gal-Yam et al. (2022). The black-solid horizontal line shows the 3σ sensitivity of NuSTAR with 400 ks exposures.

during the entire campaign with Swift reported by A. Gal-Yam et al. (2022).

For SN 2019hgp, we adopt the physical parameters from T. Nagao et al. (2023) based on the optical LC modeling: $M_{\text{ej}} = 3M_{\odot}$, $E_{\text{kin,ej}} = 2.5\text{B}$, $s = 2.9$, and $D' = 2.3$. In the

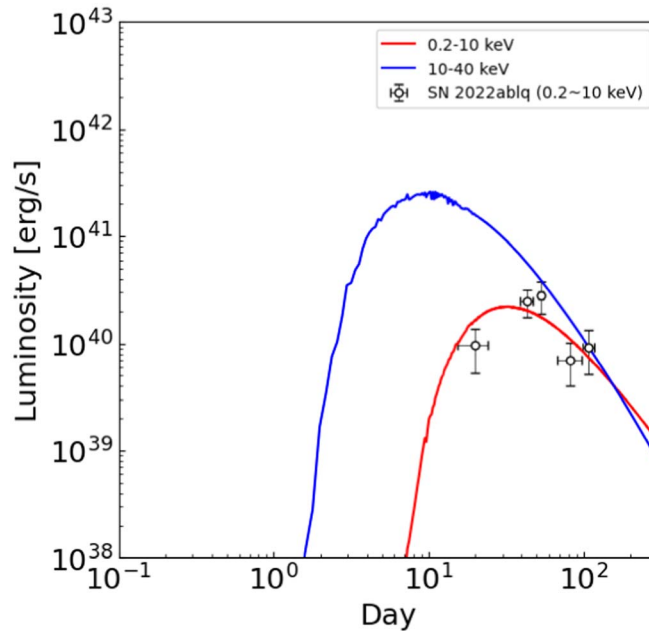


Figure 8. The synthetic hard (10–40 keV; solid-blue) and soft (0.2–10 keV; solid-red) X-ray LCs for SN 2022ablq with the (effectively) neutral unshocked CSM, as compared to the X-ray data of SN 2022ablq. Shown here is the model with (He, C, O) = (0.95, 0.025, 0.025). The data points are from the arXiv version of C. Pellegrino et al. (2024).

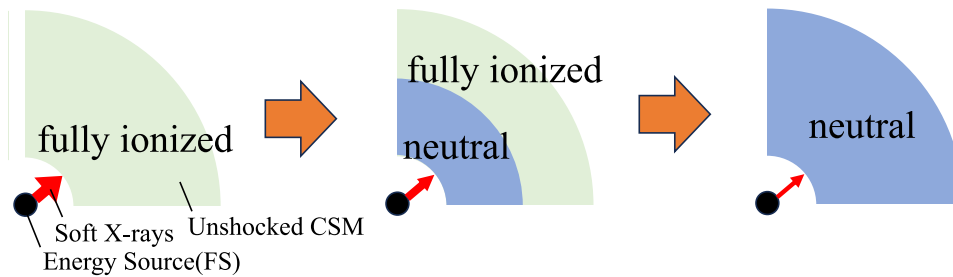


Figure 9. Schematic illustration of the photoionization change, for $\rho \propto r^{-3}$.

optical spectra, SNe Icn show lines from elements heavier than SNe Ibn, indicating He-less composition than in SNe Ibn. However, given the difficulty in deriving the He abundance in the optical spectra (e.g., L. Dessart & D. J. Hillier 2010; L. Dessart et al. 2022) and the interest in constraining the CSM composition independently from the optical spectra, we explore a range of the CSM composition; (He, C, O) = (0.85, 0.03, 0.12) (He-layer) and (0.2, 0.4, 0.4) (C-layer), as well as (C, O, Ne, Mg) = (0.05, 0.65, 0.25, 0.05) (O-core).

Figure 7 shows that all the models, including the extremely He-rich composition, are consistent with the upper limits of the soft X-ray luminosities of SN 2019hgp; unfortunately, the soft X-ray upper limits are more than an order of magnitude shallower than the required sensitivity to place a meaningful constraint on the CSM composition. Our model, on the other hand, suggests that the hard X-rays from SN 2019hgp could probably have been detected by NuSTAR with 400 ks exposure within ~ 5 –10 days; we encourage a prompt hard X-ray observation for the next nearby SN Icn.

4.3. SN 2022ablq

Figure 8 shows the synthetic X-ray LCs (with effectively neutral CSM; see Section 5) as compared to the data of SN

2022ablq taken from C. Pellegrino et al. (2024). The physical parameters adopted here are $M_{\text{ej}} = 6M_{\odot}$, $E_{\text{kin ej}} = 0.6B$, $V_{\text{CSM}} = 1500 \text{ km s}^{-1}$, $s = 3$, and $D' = 4.0$. We adopt the CSM velocity corresponding to the typical width of the helium emission lines seen in SNe Ibn (e.g., G. Hosseinzadeh et al. 2017), following C. Pellegrino et al. (2024). The adopted CSM density distribution, $s = 3$, is a typical value for SNe Ibn (K. Maeda & T. J. Moriya 2022), noting that the optical LC of SN 2022ablq is also typical (C. Pellegrino et al. 2024). We adopt (He, C, O) = (0.95, 0.025, 0.025) corresponding to the helium layer (e.g., K. Nomoto & M. Hashimoto 1988; N. Tominaga et al. 2008).

The synthetic soft X-ray LC can explain the observed X-ray LC of SN 2022ablq (see Appendix B about the robustness in deriving the CSM composition). This indicates that the CSM around SN 2022ablq contains a smaller fraction of C and O than in SN 2006jc's CSM; the shallower and outer region of the progenitor has been stripped for SN 2022ablq than SN 2006jc. To further straighten this conclusion, we emphasize again that the hard X-ray observation is important for robustly determining the CSM density profile, which is needed to derive the CSM abundance accurately by using the rising phase of the soft X-ray LC (see Sections 3.2 and 6.1).

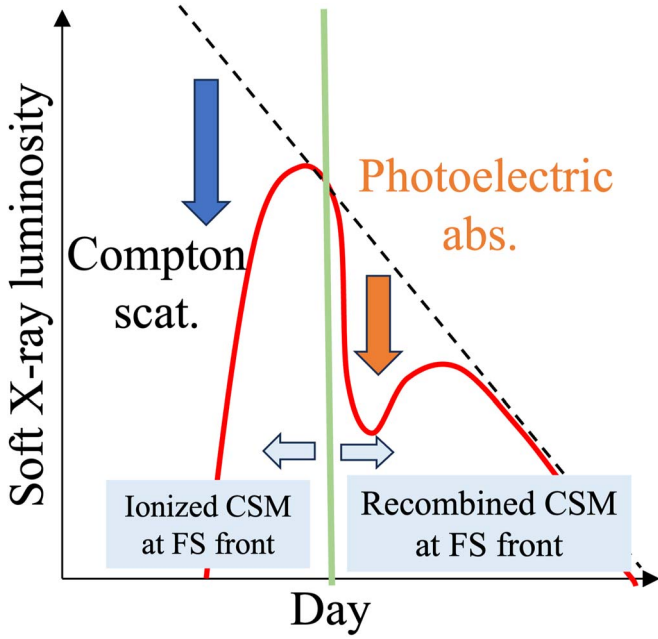


Figure 10. Schematic illustration of the double-peak soft X-ray LC. The black-dashed line shows the unabsorbed soft X-ray LC. The red-solid line shows the absorbed (observed) soft X-ray LC.

5. The Effect of Photoionization in the Unshocked CSM

5.1. Calculations of the Ionization Status

Ions in the unshocked CSM absorb soft X-rays mainly by photoelectric absorption (see Figure 3) and lose electrons in the K or L shell. Our numerical simulations in Sections 3 and 4 assume that ions in the unshocked CSM are effectively neutral for X-rays, i.e., electrons in the K or L shell are intact. In Section 5, we discuss the ionization state of the unshocked CSM, based on the ionization parameter ξ (C. B. Tarter et al. 1969; S. Hatchett et al. 1976; T. R. Kallman & R. McCray 1982; R. A. Chevalier & C. M. Irwin 2012; D. Tsuna et al. 2021). In this section's discussion, we assume that the CSM velocity and the FS velocity are constant for simplicity.

The following estimate adopts the unabsorbed X-ray luminosity as a proxy of the ionization source, and it is thus the overestimate of the ionization status by omitting the effect of the X-ray attenuation. It is thus appropriate for our main aim, i.e., to check the possible effect of the ionization to see if it would alter the conclusions obtained by the models assuming the effectively neutral CSM (Section 4).

The ionization parameter is expressed as follows:

$$\xi \text{ [erg cm s}^{-1}] = \frac{L_{X,\text{soft}}}{n_e r^2}, \quad (10)$$

where $L_{X,\text{soft}}$ and n_e are the unabsorbed soft X-ray luminosity and the number density of electrons in the unshocked CSM. The energy of photons that ionize the K-shell of C or O, as our main interest here, is mainly in the soft X-ray band.

For C or O, the K-shell electrons are lost when $\xi \gtrsim 100$ through the ionization by soft X-rays (C. B. Tarter et al. 1969; S. Hatchett et al. 1976; T. R. Kallman & R. McCray 1982; R. A. Chevalier & C. M. Irwin 2012; D. Tsuna et al. 2021). In the early epoch soon after the explosion, the soft X-ray luminosity is very large, so ξ could become larger than 100;

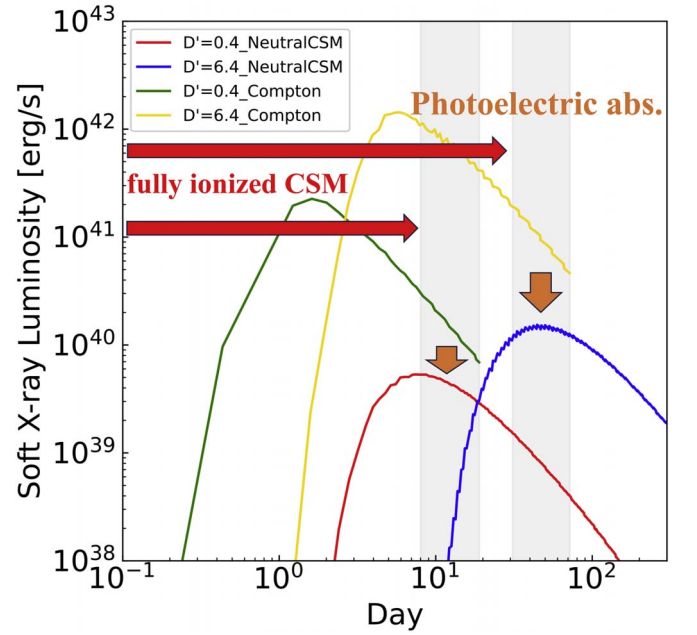


Figure 11. The soft X-ray LCs the models with for $D' = 0.4$ (red and green lines) and 6.4 (yellow and blue lines), adopting X (He) = 0.5 for CSM composition. The green and yellow lines show the synthetic LCs taking into account only Compton scattering. The red and blue lines are the synthetic LCs assuming the effectively neutral CSM. The gray area corresponds to the “recombination” period, as estimated with $\xi = 100\text{--}200$ at the unshocked CSM just ahead of the FS.

therefore C and O may be fully ionized. As time goes by, the X-ray luminosity decreases and ξ will become smaller than 100 (see Equation (11)); the K-shell electrons of C or O will then be recombined once the recombination timescale is elapsed (see Equation (12)).

Assuming $\rho \propto r^{-3}$ for the CSM density profile, the ionization parameter (Equation (10)) is expressed as follows:

$$\begin{aligned} \xi &= \frac{L_{X,\text{soft}}}{n_e r^2} \\ &\simeq \frac{L_{X,\text{soft}} \text{ [erg s}^{-1}]}{\frac{\rho_{\text{CSM}} \text{ [g cm}^{-3}] r^2 \text{ [cm}^2]}{2m_p \text{ [g]}}} \\ &\simeq 19.2 \left(\frac{L_{X,\text{soft}}}{10^{40} \text{ erg}} \right) \left(\frac{r}{10^{15} \text{ cm}} \right) \left(\frac{D' V_{\text{sh}}}{V_{\text{sh}} - V_{\text{CSM}}} \right)^{-1}. \end{aligned} \quad (11)$$

The recombination timescale $t_{\text{rec},j}$ of the element j is expressed as follows (e.g., C. Fransson 1982):

$$\begin{aligned} t_{\text{rec},j} \text{ [s]} &= (n_e \alpha(T_e))^{-1} \\ &\simeq \left(\frac{\rho_{\text{CSM}} \alpha(T_e)}{2m_p} \right)^{-1} \\ &\simeq 4 \times 10^3 \left(\frac{D'}{1} \right)^{-1} \left(\frac{r}{10^{15} \text{ cm}} \right)^3 \left(\frac{T_e}{10^6 \text{ K}} \right)^{0.5} Z_j^{-2}, \end{aligned} \quad (12)$$

where $\alpha(T_e)$ is the recombination coefficient. We note that Equation (12) ignores the CSM velocity, i.e., the recombination timescale is overestimated. However, it is justified for our purpose of confirming the assumption of the effectively neutral CSM. According to Equation (11), when $L_{X,\text{soft}}$ is fixed (i.e., if the time since the explosion is fixed), ξ is smaller for the inner region. In addition, according to Equation (12), the recombination timescale $t_{\text{rec},j}$ is shorter for the inner region. Furthermore, the optical depth of photoelectric absorption above the radius r

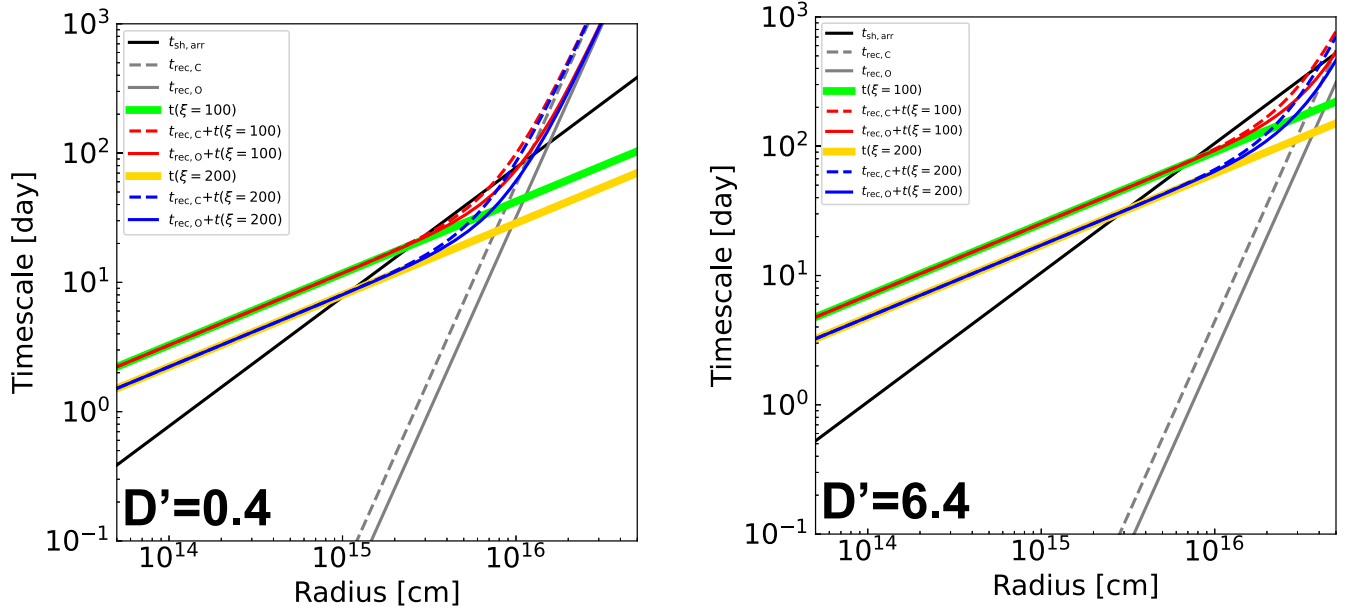


Figure 12. The diagnosing plots for the ionization state in unshocked CSM, adopting $D' = 0.4$ (left) and 6.4 (right). The lines correspond to various timescales (see the legend). We assume $T_e = 10^6$ K (e.g., C. Fransson et al. 1996). For $D' = 0.4$ (left), we adopt the following conditions: $V_{\text{sh}} = 1.5 \times 10^9$ cm s $^{-1}$, and $L_{X,\text{soft}} = 2.0 \times 10^{40} \left(\frac{t}{10 \text{ days}}\right)^{-1.8}$ erg s $^{-1}$ (see Figure 11). For $D' = 6.4$ (right), we adopt the following conditions: $V_{\text{sh}} = 1.1 \times 10^9$ cm s $^{-1}$, and $L_{X,\text{soft}} = 2.0 \times 10^{40} \left(\frac{t}{100 \text{ days}}\right)^{-1.8}$ erg s $^{-1}$ (see Figure 11).

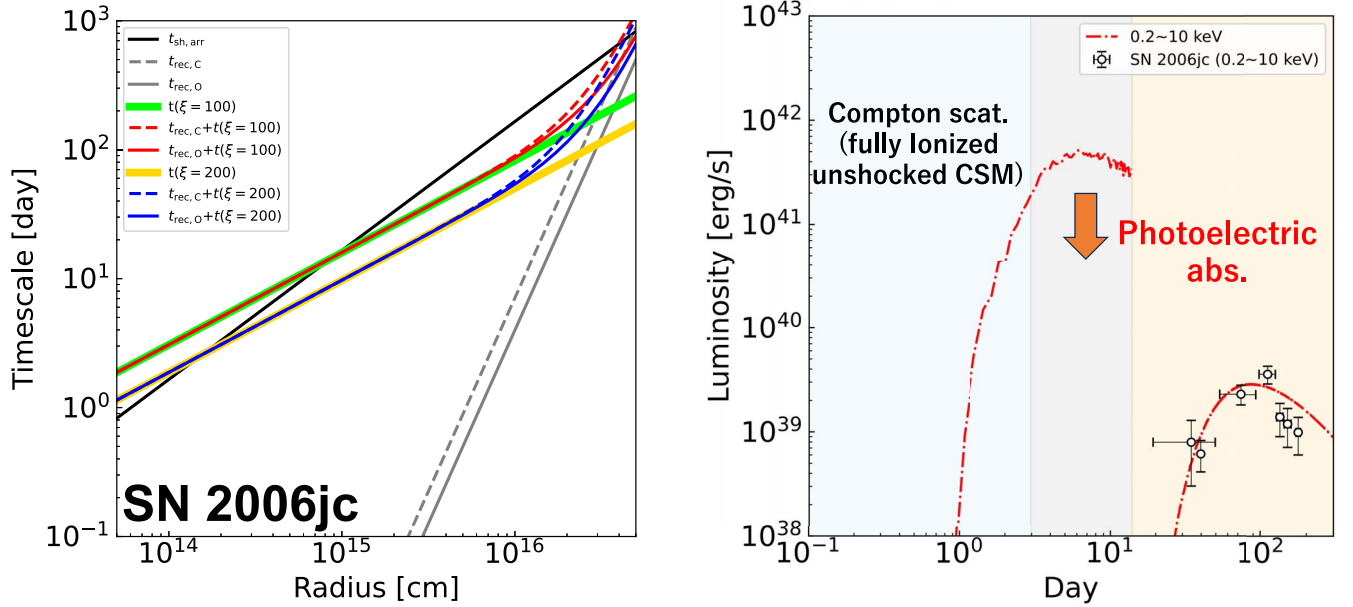


Figure 13. The left panel shows the diagnosing plot for the ionization state in the unshocked CSM of SN 2006jc (see the caption of Figure 12). We adopt the following conditions: $V_{\text{sh}} = 0.7 \times 10^9$ cm s $^{-1}$, and $L_{X,\text{soft}} = 2.0 \times 10^{40} \left(\frac{t}{100 \text{ days}}\right)^{-1.4}$ erg s $^{-1}$. The right panels show the model for the absorbed (observed) soft X-ray LC of SN 2006jc (red lines), as compared to the observed data points for SN 2006jc taken from S. Immler et al. (2008). In the earliest phase (blue area), the soft X-ray luminosity is computed by taking into account only Compton scattering. In the orange area, the soft X-ray luminosity is computed by taking into account photoelectric absorption on the effectively neutral CSM. The gray area corresponds to the recombination period as estimated with $\xi = 100$ –200 for the critical ionization parameter.

is expressed as $\tau \propto r^{-2}$. Summarizing these conditions, the ionization state at the FS front essentially determines whether photoelectric absorption is important or not (see Figure 9). Therefore, in the following discussion, we focus on the ionization state at the FS front.

Here, we discuss the ionization state at radius r . We define $t_{\text{sh,arr}}$ as the time for the FS to reach r ;

$$t_{\text{sh,arr}} = \frac{r}{V_{\text{sh}}}. \quad (13)$$

At time $t_{\text{sh,arr}}$, the criterion that photoelectric absorption is important is expressed as follows:

$$t_{\text{rec},j}(r) + t(\xi \simeq 100; \text{ at } r) < t_{\text{sh,arr}}, \quad (14)$$

where $t(\xi \simeq 100; \text{ at } r)$ is the time since the explosion when ξ at r has decreased to 100. If this relation is satisfied, the CSM at r is recombined before the FS reaches there, providing the source of photoelectric absorption. We note that the recombination time is negligible as compared to $t(\xi \simeq 100; \text{ at } r)$ in the early phase, and thus for our purpose the recombination timescale can be practically omitted from Equation (14). We note that the critical value set as $\xi \simeq 100$ is a rough estimate, and indeed can be an underestimate (S. Hatchett et al. 1976); we thus adopt a range of $\xi = 100\text{--}200$ in the subsequent discussion.

In the earliest epoch of SNe Ibn/Icn, it is possible that Equation (14) is not satisfied because the soft X-ray luminosity could be very large. Then, the CSM is likely fully ionized at the FS front, and whether the soft X-rays can escape or is not determined by photoelectric absorption but by Compton scattering. This will generally lead to more luminous soft X-ray emission than computed in Sections 3 and 4 in the earliest epoch.

If Equation (14) is satisfied at the FS front before the soft X-ray peak time computed without the ionization effect (see Sections 3 and 4), the “real” soft X-ray LC, taking into account the ionization effect, could show double peaks as demonstrated in Figure 10. In this case, the soft X-rays can escape initially through the fully ionized CSM in the earliest phase. As time passes, the unabsorbed X-ray emission becomes weak and the ions in the unshocked CSM start recombining. Then, the optical depth suddenly increases due to the photoelectric absorption, leading to a sharp dimming of the soft X-ray LC. Once the FS front becomes effectively neutral, the optical depth to the photoelectric absorption will simply decrease, thus the soft X-ray LC will rise again toward the (second) peak.

5.2. Double-peaked Soft X-Ray LCs

We apply the photoionization model in Section 5.1 to the models with $D' = 0.4$ and 6.4 (Figure 11 for the “neutral” CSM). The timescales mentioned in Section 5.1 are shown in Figure 12. Figure 12 shows that Equation (2, 14) is satisfied in the time window at > 8 ($\xi = 200$) or > 19 ($\xi = 100$) days ($D' = 0.4$), or > 31 ($\xi = 200$) or > 72 ($\xi = 100$) days ($D' = 6.4$). The peak dates computed for the “neutral” CSM are in these time windows (Figure 11; ~ 8 days for $D' = 0.4$ and ~ 50 days for $D' = 6.4$). The analysis here demonstrates that the assumption of the neutral CSM is not necessarily correct in the early phase, and the effect of the ionization should be checked in studying individual objects. Further, the ionization effect can create a unique soft X-ray evolution, i.e., the double peaks (or a peak followed by a shoulder), demonstrating the importance of prompt soft X-ray observations in the early phase (see Figure 11).

5.3. Revisiting the Soft X-Ray Emissions from SNe 2006jc, 2019hgp, and 2022ablq

The soft X-ray data of SN 2006jc in the range of $\sim 20\text{--}200$ days were fit in Section 4.1, assuming that the unshocked CSM was already recombined in these epochs. In estimating the effect of the ionization for SN 2006jc, we approximate its unabsorbed

soft X-ray luminosity as $L_{X,\text{soft}} = 2 \times 10^{40} \left(\frac{t}{100 \text{ days}} \right)^{-1.4} \text{ erg s}^{-1}$ (Figure 6) and its shock velocity as $V_{\text{sh}} = 0.7 \times 10^9 \text{ cm s}^{-1}$ (as given by SNEC). Adopting the same model parameters as those shown in Figure 6, the diagnosing plots for the ionization status are shown in the right panel in Figure 13. We estimate the inner-shell electrons of C and O in the FS front are recombined between the first 3 ($\xi = 200$) and 14 ($\xi = 100$) days since the explosion, after which photoelectric absorption is expected to fully operate as was assumed in Section 4.1. In addition to this confirmation, the analysis here provides an interesting implication; our model predicts that a bright soft X-ray might have been associated with SN 2006jc within the first 3 ($\xi = 200$) or 14 ($\xi = 100$) days (left panel in Figure 13), if it were observed in the soft X-ray band promptly just after the explosion.

We have done the same exercises for SNe 2019hgp and 2022ablq (Figures 7 and 8). We adopt $L_{X,\text{soft}} = 3.0 \times 10^{39} \left(\frac{t}{100 \text{ days}} \right)^{-1.7} \text{ erg s}^{-1}$ and $V_{\text{sh}} = 1.7 \times 10^9 \text{ cm s}^{-1}$ for SN 2019hgp; $L_{X,\text{soft}} = 1.2 \times 10^{40} \left(\frac{t}{100 \text{ days}} \right)^{-1.7} \text{ erg s}^{-1}$ and $V_{\text{sh}} = 0.55 \times 10^9 \text{ cm s}^{-1}$ for SN 2022ablq. The relatively low FS velocity adopted here is consistent with the shock velocity of SN 2022ablq estimated by C. Pellegrino et al. (2024). We find that photoelectric absorption starts attenuating the soft X-ray at ~ 5 ($\xi = 200$) or ~ 15 ($\xi = 100$) days for SN 2022ablq (Figure 14). The phase is before the first X-ray detection, confirming the consistency of our derived parameters for SN 2022ablq in Section 4.3 with the X-ray observation.)

A possible issue is raised for the ionization effect for SN 2019hgp. We find that photoelectric absorption starts attenuating the soft X-ray between 13 and 28 days for SN 2019hgp (see Figure 15), thus the expected early “bright” phase overlaps with part of the periods when it was observed by Swift resulting in non-detection (A. Gal-Yam et al. 2022). With the ionization effect considered here, we indeed expect that it should have been detected (Figure 15). This might demonstrate several limitations in the present analysis, including the following: there is uncertainty in the physical parameters estimated by the optical LC modeling. The earliest epoch at $\lesssim 4$ days might be contaminated by an LC component other than the interaction, and it is beyond the applicability of the optical LC modeling presented in T. Nagao et al. (2023; see Figure 4 of T. Nagao et al. 2023); without detection, deriving the X-ray luminosity upper limit involves uncertainties (e.g., assumed SED); we might overestimate the ionization effect by ignoring the effect of the attenuation of X-rays. To settle this issue, more detailed calculations, including the attenuation effect, are needed, together with the detection of the hard X-rays (to accurately derive the physical parameters such as the CSM density; see Section 6.1) and the soft X-rays (to calibrate the model).

6. Discussion

6.1. The Importance of Hard X-Ray Observation

Deriving the CSM composition (e.g., SNe 2006jc and 2022ablq in Section 4.1) is influenced by the assumed CSM density distribution. This is because the rising properties of the soft X-ray LC are controlled by the column density of heavier elements that are determined by the CSM density and composition, as shown in Equation (9). Here is where the hard X-ray LC provides independent and powerful diagnostics; even in the rising phase of the soft X-ray LC, the hard X-rays can already be in the optically thin phase, and it can provide a

robust measure of the CSM density parameters (D' and s). The CSM abundance can then be derived through the soft X-ray LC analysis. Given its nature as a bolometer of the SN-CSM interaction energetics, the hard X-ray LC is a more direct trace of the CSM density properties than in the optical LC analysis.

As shown in Figure 7, NuSTAR provides a sensitivity that is expected to be sufficient to detect nearby SNe Ibn/Icn in hard X-rays, if the observation is performed promptly after the explosion. This will provide a key contribution to studying the progenitor of SNe Ibn/Icn and their final activities.

6.2. Possible Effects of Inverse Compton Scattering

According to the previous study (K. Maeda & T. J. Moriya 2022), the main energy source of the optical photon is provided by the inward-going X-rays originally emitted at the FS, which are then reprocessed into the optical photons either in the FS, RS or the unshocked ejecta. The outward-going optical photons then inversely pass through the outer layers, such as the RS or FS, and may experience inverse Compton scattering by these regions and be energized to X-rays. However, when a non-negligible fraction of X-rays can escape the shocked regions, the system should also be optically thin to optical photons. Therefore, the contribution of the X-ray photons created through inverse Compton scattering by thermal electrons will not be a main contributor to the X-ray LC.

In addition, we note that our model does not treat nonthermal (relativistic) electrons, which are generated at the FS front through the diffusive shock acceleration mechanism. In some situations, inverse Compton scattering of optical photons by these nonthermal electrons could contribute to the X-ray emission (see, e.g., A. R. Bell 1978a, 1978b; L. O. Drury 1983; C. Fransson & C. -I. Björnsson 1998; R. A. Chevalier & C. Fransson 2003, 2017; K. Maeda 2012, 2013; T. Matsuoka et al. 2019; K. Murase et al. 2019, about charged particle acceleration at the shock front). In an extreme circumstance, synchrotron emission could directly contribute to X-ray emission (e.g., K. Murase et al. 2019). While the particle acceleration process (e.g., E. Fermi 1949; A. R. Bell 1978a, 1978b; L. O. Drury 1983) and the efficiency are still under debate, for the high-density CSM considered here, this will be overwhelmed by the thermal X-ray emission (e.g., K. Maeda et al. 2014). One possible exception is the late-time tail phase, where the efficiency of the thermal X-ray emission decreases due to the rapidly decreasing CSM density for SNe Ibn/Icn; this is an issue we plan to investigate in the future.

7. Summary

In the present study, we have developed an X-ray LC model for SNe Ibn/Icn, taking into account the rapid cooling behind the FS as a post-process (Section 2). Through studying the parameter dependence on the resulting emission (Section 3), our findings can be summarized as follows:

1. The hard X-ray LC provides a robust measure of the explosion properties (E_{ej} , M_{ej}) and the CSM density distribution (ρ_{CSM}), as a tracer of the SN-CSM interaction energetics.
2. The soft X-ray LC is important for revealing the CSM composition, thanks to its rising LC properties controlled by the photoelectric absorption in the unshocked CSM.

3. Therefore, broadband X-ray observation is required to robustly reveal the nature of the progenitor and its final activities.

We have then applied our X-ray LC model to the observational data of SNe 2006jc, 2019hgp, and 2022ablq. Under the assumption of the effectively neutral CSM (where the inner-shell electrons of carbon/oxygen are bound), the results can be summarized as follows:

1. The X-ray LC of SN 2006jc can be explained by the physical parameters derived from the optical LC modeling: $M_{ej} = 6M_{\odot}$, $E_{kin\ ej} = 0.8B$, $V_{CSM} = 3000\text{ km s}^{-1}$, $s = 3$, and $D' = 4.0$. In addition, the X-ray LC of SN 2022ablq can be explained by the physical parameters of typical SNe Ibn derived from the optical LC modeling: $M_{ej} = 6M_{\odot}$, $E_{kin\ ej} = 0.6B$, $V_{CSM} = 1500\text{ km s}^{-1}$, $s = 3$, and $D' = 4.0$. These demonstrate a general consistency between the optical and X-ray properties on the basis of the SN-CSM interaction model, supporting the interaction scenario to explain the nature of SNe Ibn (and Icn).
2. Our model indicates the difference in the CSM compositions between SNe 2006jc and 2022ablq despite their both being SNe Ibn; (He, C, O) = (0.4, 0.3, 0.3) for SN 2006jc and (He, C, O) = (0.95, 0.025, 0.025) for 2022ablq, respectively (see Appendix B about the robustness in deriving the CSM composition). This indicates that even within the same SN Ibn class, there could be a diversity in the degree of the mass loss and envelope stripping; the mass loss of the SN 2006jc progenitor might have reached down nearly to the bottom of the He envelope, while SN 2022ablq progenitor might have experienced a less extreme stripping where the stripping has been reached to the middle of the He layer.
3. However, the above conclusion on the CSM composition should not be overinterpreted, and will require further confirmation; it depends on the assumed CSM density distribution. A more robust estimate of the CSM composition can be obtained by adding the hard X-ray observation and modeling, highlighting the importance of the prompt hard X-ray follow-up observation.
4. The soft X-ray upper limit for SN 2019hgp as obtained by Swift is consistent with the interaction model, and indeed consistent with any CSM compositions examined in the present work.
5. While the hard X-ray observation has not been reported for SN 2019hgp, our model predicts that it must have been detected if a prompt observation just after the discovery were conducted by NuSTAR.

The assumption that the inner-shell electrons of carbon/oxygen are bound affects the strength of photoelectric absorption. We have further explored the effect of photoionization of the unshocked CSM by the X-ray emitted from the interacting region on the emerging soft X-rays:

1. In a few days since the explosion, we may indeed expect strong soft X-ray emission; the unshocked CSM just ahead of the FS is expected to be fully ionized due to high X-ray luminosity.
2. As combined with “the second peak,” as created through suppression of the soft X-ray once the CSM is recombined and then the rising LC as the column density

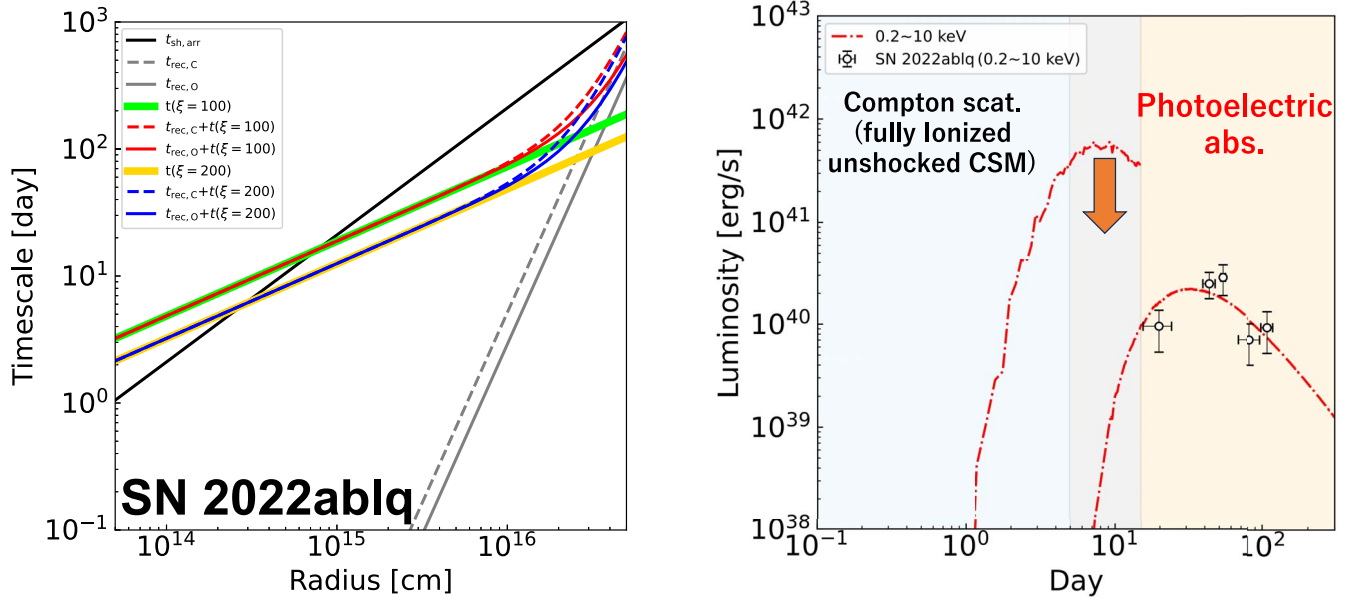


Figure 14. The left panel shows the diagnosing plot for the ionization state in the unshocked CSM of SN 2022ablq. We adopt the following conditions: $V_{sh} = 0.55 \times 10^9 \text{ cm s}^{-1}$, and $L_{X,soft} = 1.2 \times 10^{40} \left(\frac{t}{100 \text{ days}}\right)^{-1.7} \text{ erg s}^{-1}$. The right panels show the model for the absorbed (observed) soft X-ray LC of SN 2022ablq (red lines), as compared to the observed data points taken from the arXiv version of C. Pellegrino et al. (2024). See the caption of Figure 13.

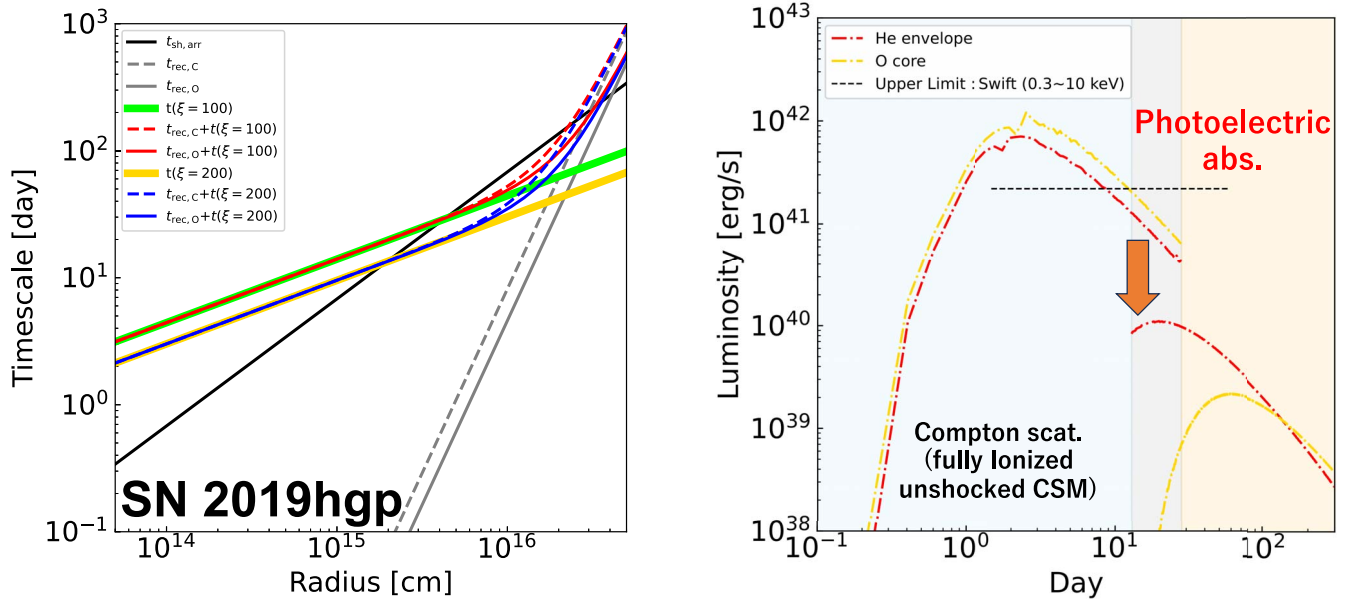


Figure 15. The left panel shows the diagnosing plot for the ionization state in the unshocked CSM of SN 2019hgp. We adopt the following conditions: $V_{sh} = 1.7 \times 10^9 \text{ cm s}^{-1}$, and $L_{X,soft} = 3.0 \times 10^{39} \left(\frac{t}{100 \text{ days}}\right)^{-1.7} \text{ erg s}^{-1}$. The right panels show the model for the absorbed (observed) soft X-ray LC of SN 2019hgp adopting the “He-envelope” compositions (dashed-red) and the “O-core” compositions (dashed-yellow; see Section 4.2). The upper limit of the soft X-ray luminosity of SN 2019hgp is taken from A. Gal-Yam et al. (2022). See the caption of Figure 13.

decreases, we show that SNe Ibn/Icn may show double-peaked soft X-ray LC.

- For the models adopted for SNe 2006jc and 2022ablq, we have confirmed that the assumption of the effectively neutral CSM is appropriate in the epochs where the soft X-ray data are available (i.e., in the second peak).
- In addition to the hard X-ray observation, the prompt soft X-ray observation within a few days can thus be a new

window to study the nature of the SNe Ibn/Icn progenitors and their final activities.

- Indeed, our tentative analysis of SN 2019hgp, we estimate that soft X-ray should have been detected in the earliest phase despite the non-detection by Swift. This demonstrates a possibility of further refining the model and constraining the nature of SNe Ibn/Icn. For more accurate calculations of photoelectric absorption, the simple treatment of ionization states of ions in the present

study should be updated, and the attenuation of X-rays in the radial direction, which is related to the photoionization of ions, needs to be included.

Acknowledgments

The authors thank Shiu-Hang Lee, Tatsuya Matsumoto, Daichi Hiramatsu, Kenta Taguchi, Kohki Uno, and Masaki Tsurumi for the fruitful discussions. Y.I. acknowledges supported by a grant from the Hayakawa Satio Fund awarded by the Astronomical Society of Japan. K.M. acknowledges support from the JSPS KAKENHI grants JP20H00174, JP24H01810, and 24KK0070.

Appendix A

Feedback of Radiation Loss on Hydrodynamics

The present model does not consider feedback of radiative loss on hydrodynamics. To investigate the influence of radiative cooling on hydrodynamics, radiation hydrodynamic (RH) simulations using SNEC are conducted with the most extreme model with $D' = 6.4$ (see Section 3 for the other parameters). We note that the SNEC assumes complete thermal equilibrium and blackbody radiation, which leads to an overestimation of the influence of the radiation loss. We find that the RH simulation by SNEC results in a 20% reduction in the shock velocity and a 100% enhancement in the gas density behind the shock, as compared to the adiabatic hydrodynamic simulation. The relation between X-ray luminosity and the properties behind the FS is expressed as follows:

$$L_X \propto T^{0.5} \rho^2 \text{Vol}_{\text{FS}} \propto V_{\text{sh}}^4 \rho^2, \quad (\text{A1})$$

where T , ρ , and Vol_{FS} are gas temperature, mass density, and volume of the region shocked by the FS. According to Equation (A1), the resulting X-ray luminosity is increased by 60% as compared to the adiabatic hydrodynamic simulation. Therefore, the synthetic unabsorbed X-ray luminosity in the present study might be underestimated by a factor of at most 1.6 by neglecting the feedback effect.

The optical depth is expressed as follows:

$$\begin{aligned} \tau_{\text{pe}}, \tau_{\text{comp}} &\propto r_{\text{sh}}^{-s+1} \quad (\text{for } s > 1) \\ &\propto V_{\text{sh}}^{-s+1}. \end{aligned} \quad (\text{A2})$$

According to Equation (A2), the RH simulation for the model with $D' = 6.4$ and $s = 3$ provides 60% higher optical depth than that provided by the adiabatic hydrodynamics simulation. Given that the model examined here sets basically the upper limit on the feedback effect. Our X-ray LC model in the main text (Section 2) underestimates the optical depth by at most a factor of 1.6.

Appendix B

Robustness in Deriving the CSM Composition

To discuss the robustness in deriving the CSM compositions in Sections 4.1 and 4.3, we show the synthetic soft X-ray LCs with several models with different CSM compositions, as compared to the data of SNe 2006jc and 2022ablq in Figures 16 and 17, respectively. Thanks to the data point of SN 2006jc at ~ 40 days since the explosion, we find that our X-ray LC model prefers the low helium composition models (e.g., 20%, 30%, and 40% models). In addition, considering the peak soft X-ray data point of SN 2006jc, we conclude that the

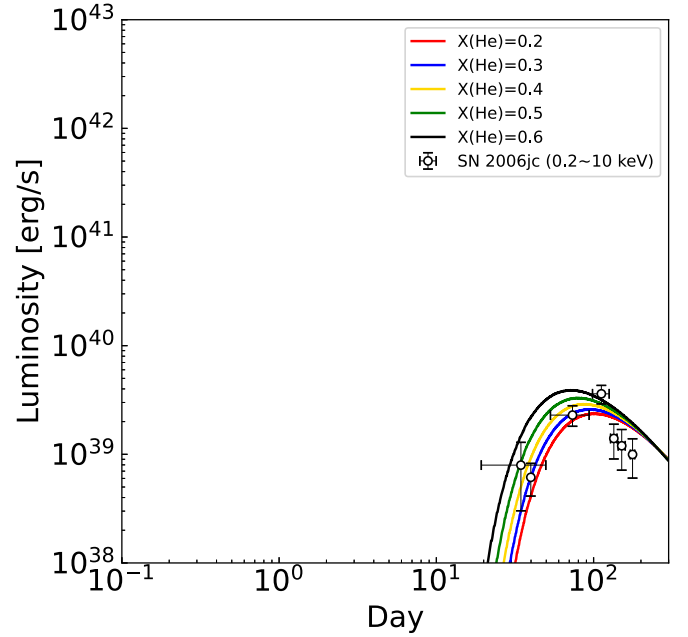


Figure 16. The synthetic soft (0.2–10 keV) X-ray LCs for SN 2006jc with the (effectively) neutral unshocked CSM, as compared to the X-ray data of SN 2006jc. Shown here are the models with (He, C, O) = (0.2, 0.4, 0.4) (red), (He, C, O) = (0.3, 0.35, 0.35) (blue), (He, C, O) = (0.4, 0.3, 0.3) (yellow), (He, C, O) = (0.5, 0.25, 0.25) (green), and (He, C, O) = (0.6, 0.2, 0.2) (black). The data points are from S. Immler et al. (2008).

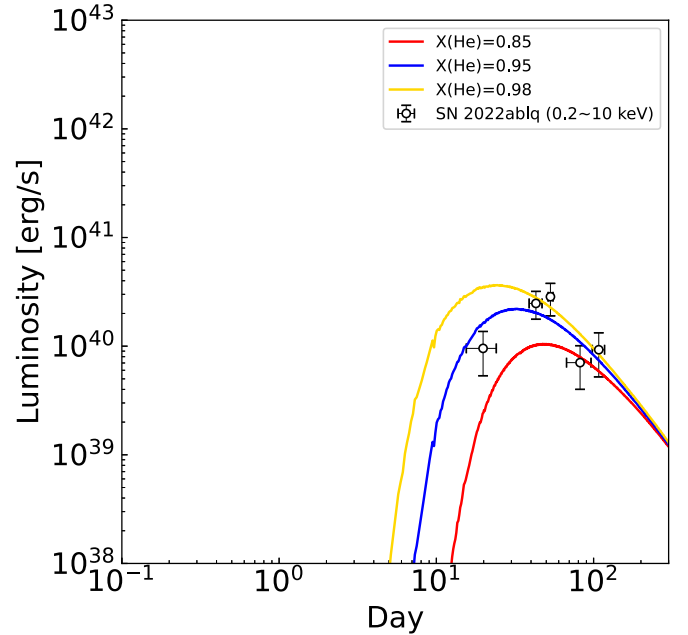


Figure 17. The synthetic soft (0.2–10 keV) X-ray LCs for SN 2022ablq with the (effectively) neutral unshocked CSM, as compared to the X-ray data of SN 2022ablq. Shown here are the models with (He, C, O) = (0.85, 0.075, 0.075) (red), (He, C, O) = (0.95, 0.025, 0.025) (blue), and (He, C, O) = (0.98, 0.01, 0.01) (yellow). The data points are from the arXiv version of C. Pellegrino et al. (2024).

40% helium model is plausible for the CSM composition of SN 2006jc. Similar to the discussion of SN 2006jc, from the data points in the rising phase and the peak phase, we conclude that the 95% helium model is plausible for the CSM composition of SN 2022ablq.

ORCID iDs

Yusuke Inoue  <https://orcid.org/0009-0004-3148-0462>
 Keiichi Maeda  <https://orcid.org/0000-0003-2611-7269>

References

- Bell, A. R. 1978a, *MNRAS*, **182**, 147
 Bell, A. R. 1978b, *MNRAS*, **182**, 443
 Brennan, S. J., Sollerman, J., Irani, I., et al. 2024, *A&A*, **684**, L18
 Brunetti, A., Sanchez del Rio, M., Golosio, B., Simionovici, A., & Somogyi, A. 2004, *AcSpB*, **59**, 1725
 Chandra, P., Chevalier, R. A., Chugai, N., et al. 2012, *ApJ*, **755**, 110
 Chevalier, R. A. 1982, *ApJ*, **258**, 790
 Chevalier, R. A., & Fransson, C. 2003, in *Supernovae and Gamma-Ray Bursters*, ed. K. Weiler (Berlin: Springer), 171
 Chevalier, R. A., & Fransson, C. 2006, *ApJ*, **651**, 381
 Chevalier, R. A., & Fransson, C. 2017, in *Handbook of Supernovae*, ed. A. W. Alsabti & P. Murdin (Berlin: Springer), 875
 Chevalier, R. A., & Irwin, C. M. 2012, *ApJL*, **747**, L17
 Chugai, N. N. 2009, *MNRAS*, **400**, 866
 Cox, D. P., & Tucker, W. H. 1969, *ApJ*, **157**, 1157
 Davis, K. W., Taggart, K., Tinyanont, S., et al. 2023, *MNRAS*, **523**, 2530
 Dessart, L., & Hillier, D. J. 2010, *MNRAS*, **405**, 2141
 Dessart, L., Hillier, D. J., & Kuncarayakti, H. 2022, *A&A*, **658**, A130
 Drury, L. O. 1983, *RPPH*, **46**, 973
 Fermi, E. 1949, *PhRv*, **75**, 1169
 Filippenko, A. V. 1997, *ARA&A*, **35**, 309
 Foley, R. J., Smith, N., Ganeshalingam, M., et al. 2007, *ApJL*, **657**, L105
 Fransson, C. 1982, *A&A*, **111**, 140
 Fransson, C., & Björnsson, C.-I. 1998, *ApJ*, **509**, 861
 Fransson, C., Ergon, M., Challis, P. J., et al. 2014, *ApJ*, **797**, 118
 Fransson, C., Lundqvist, P., & Chevalier, R. A. 1996, *ApJ*, **461**, 993
 Gal-Yam, A., Bruch, R., Schulze, S., et al. 2022, *Natur*, **601**, 201
 Gal-Yam, A., Yaron, O., Pastorello, A., et al. 2021, *TNSAN*, **76**, 1
 Gangopadhyay, A., Misra, K., Hiramatsu, D., et al. 2020, *ApJ*, **889**, 170
 Hatchett, S., Buff, J., & McCray, R. 1976, *ApJ*, **206**, 847
 Hosseinzadeh, G., Arcavi, I., Valenti, S., et al. 2017, *ApJ*, **836**, 158
 Immler, S., Modjaz, M., Landsman, W., et al. 2008, *ApJL*, **674**, L85
 Itoh, H. 1977, *PASJ*, **29**, 813
 Kallman, T. R., & McCray, R. 1982, *ApJS*, **50**, 263
 Longair, M. S. 2011, *High Energy Astrophysics* (Cambridge: Cambridge Univ. Press)
 Maeda, K. 2012, *ApJ*, **758**, 81
 Maeda, K. 2013, *ApJ*, **762**, 14
 Maeda, K., Katsuda, S., Bamba, A., Terada, Y., & Fukazawa, Y. 2014, *ApJ*, **785**, 95
 Maeda, K., & Moriya, T. J. 2022, *ApJ*, **927**, 25
 Matsuoka, T., Maeda, K., Lee, S.-H., & Yasuda, H. 2019, *ApJ*, **885**, 41
 Mattila, S., Meikle, W. P. S., Lundqvist, P., et al. 2008, *MNRAS*, **389**, 141
 Moriya, T. J., & Maeda, K. 2016, *ApJ*, **824**, 100
 Moriya, T. J., Maeda, K., Taddia, F., et al. 2013, *MNRAS*, **435**, 1520
 Moriya, T. J., Maeda, K., Taddia, F., et al. 2014, *MNRAS*, **439**, 2917
 Morozova, V., Piro, A. L., Renzo, M., et al. 2015, *ApJ*, **814**, 63
 Murase, K., Franckowiak, A., Maeda, K., Margutti, R., & Beacom, J. F. 2019, *ApJ*, **874**, 80
 Nagao, T., Kuncarayakti, H., Maeda, K., et al. 2023, *A&A*, **673**, A27
 Nomoto, K., & Hashimoto, M. 1988, *PhR*, **163**, 13
 Nozawa, T., Kozasa, T., Tominaga, N., et al. 2008, *ApJ*, **684**, 1343
 Ofek, E. O., Cameron, P. B., Kasliwal, M. M., et al. 2007, *ApJL*, **659**, L13
 Ofek, E. O., Zoglauer, A., Boggs, S. E., et al. 2014, *ApJ*, **781**, 42
 Pastorello, A., Mattila, S., Zampieri, L., et al. 2008, *MNRAS*, **389**, 113
 Pastorello, A., Smartt, S., & Mattila, S. e. a. 2007, *Natur*, **447**, 829832
 Pellegrino, C., Howell, D. A., Terreran, G., et al. 2022a, *ApJ*, **938**, 73
 Pellegrino, C., Howell, D. A., Vinkó, J., et al. 2022b, *ApJ*, **926**, 125
 Pellegrino, C., Modjaz, M., Takei, Y., et al. 2024, *ApJ*, **977**, 2
 Perley, D. A., Sollerman, J., Schulze, S., et al. 2022, *ApJ*, **927**, 180
 Pursiainen, M., Leloudas, G., Schulze, S., et al. 2023, *ApJL*, **959**, L10
 Rybicki, G. B., & Lightman, A. P. 1979, *Radiative Processes in Astrophysics* (New York: Wiley)
 Sakon, I., Onaka, T., Wada, T., et al. 2009, *ApJ*, **692**, 546
 Schoonjans, T., Brunetti, A., Golosio, B., et al. 2011, *AcSpB*, **66**, 776
 Shivvers, I., Zheng, W. K., Mauerhan, J., et al. 2016, *MNRAS*, **461**, 3057
 Shivvers, I., Zheng, W., Van Dyk, S. D., et al. 2017, *MNRAS*, **471**, 4381
 Smith, N. 2014, *ARA&A*, **52**, 487
 Smith, N. 2017, in *Handbook of Supernovae*, ed. A. W. Alsabti & P. Murdin (Berlin: Springer), 403
 Smith, N., Li, W., Foley, R. J., et al. 2007, *ApJ*, **666**, 1116
 Stritzinger, M., Taddia, F., Fransson, C., et al. 2012, *ApJ*, **756**, 173
 Sun, N.-C., Maund, J. R., Hirai, R., Crowther, P. A., & Podsiadlowski, P. 2020, *MNRAS*, **491**, 6000
 Tarter, C. B., Tucker, W. H., & Salpeter, E. E. 1969, *ApJ*, **156**, 943
 Tominaga, N., Limongi, M., Suzuki, T., et al. 2008, *ApJ*, **687**, 1208
 Tsuna, D., Kashiyama, K., & Shigeyama, T. 2021, *ApJ*, **914**, 64